Nano Research

Open Access

Research Article

Harnessing HSPB1-targeted radiotheranostics for early diagnosis and precision therapy in colorectal cancer

Shu Liu[1,§], Yuhong Wang[2,§], Mengmeng Xu[3,§], Chonghai Zhang[1], Xulu Yang[1], Fei Peng[2], Huan Yang[2], Teng Liu[1], Weifeng Li[4], Judong Luo[5], Kai Yang[1] ✉, and Lin Hu[1] ✉

[1] *Department of Pathology, the First Affiliated Hospital, State Key Laboratory of Radiation Medicine and Protection, School of Radiation Medicine and Protection & School for Radiological and Interdisciplinary Sciences (RAD-X), Collaborative Innovation Center of Radiation Medicine of Jiangsu Higher Education Institutions, Soochow University, Suzhou 215123, China*
[2] *Department of Pathology, The First Affiliated Hospital of Soochow University, Suzhou 215000, China*
[3] *Department of Pathology, The Second Affiliated Hospital of Soochow University, Suzhou 215004, China*
[4] *School of Physics, Shandong University, Jinan 250100, China*
[5] *Department of Radiotherapy, Tongji Hospital, School of Medicine, Tongji University, Shanghai 200065, China*
§ *Shu Liu, Yuhong Wang, and Mengmeng Xu contributed equally to this work.*

Cite this article: *Nano Research*, **2026**, *19*, 94908439. https://doi.org/10.26599/NR.2026.94908439

ABSTRACT: Colorectal cancer (CRC) has high global incidence and mortality, yet effective diagnostic tools for detecting the adenoma to adenocarcinoma transition are lacking, making identification of adenomas with malignant transformation potential essential for early diagnosis and intervention. This study aimed to identify key biomarkers involved in the adenoma-carcinoma sequence. Based on this discovery, we developed an integrated radionuclide probe for diagnosis and therapy. Through a combination of retrospective clinical analysis, proteomics, and cellular experiments, we identified a significant upregulation of heat shock protein beta-1 (HSPB1) during the adenoma–carcinoma transition, which is closely associated with tumor proliferation, invasiveness, and metastatic potential. Based on this finding, we constructed HSPB1-targeted radiolabeled probes—^{177}Lu-DPTP. *In vitro* and *in vivo*, including early CRC patient-derived xenograft (PDX) and low rectal cancer models, ^{177}Lu-DPTP demonstrates high targeting specificity and favorable pharmacokinetics, selectively accumulates in HSPB1-high tumors, and produces effective imaging and therapeutic outcomes. It enabled non-invasive diagnosis via molecular imaging while significantly inhibiting tumor growth through targeted radiotherapy, without notable toxicity. In conclusion, our study highlights the pivotal role of HSPB1 in colorectal adenoma–carcinoma progression and demonstrates the potential of HSPB1-targeted probes for early diagnosis and precision therapy of CRC, offering a promising strategy for improved screening and treatment outcomes.

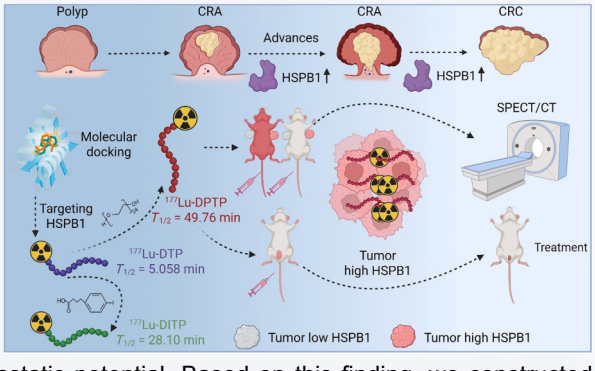

KEYWORDS: radionuclide, theranostics, heat shock protein beta-1 (HSPB1), PEGylation, adenoma–carcinoma transformation

1 Introduction

Colorectal cancer (CRC) is one of the most prevalent malignancies worldwide, originating from malignant transformation of the epithelial cells lining the colon or rectum. It accounts for approximately 10% of all cancer cases and 9.4% of cancer-related deaths globally [1, 2]. Colorectal adenomas are recognized as the principal precancerous lesions of CRC. Although the overall malignant transformation rate of colorectal adenomas is relatively low, the molecular mechanisms underlying this transformation remain incompletely understood. Previous studies have suggested that the adenoma–carcinoma sequence involves a complex array of molecular events, including genetic mutations, epigenetic alterations, and aberrant activation of the immune microenvironment [3–5]. However, in-depth investigations into the role of specific key molecules during this progression are still lacking.

Received: October 8, 2025; **Revised:** January 10, 2026
Accepted: January 13, 2026

✉Address correspondence to Kai Yang, kyang@suda.edu.cn; Lin Hu, hulin@suda.edu.cn

Several screening modalities have been developed for early diagnosis to reduce CRC mortality. These include non-invasive tests like the fecal occult blood test (FOBT) and liquid biopsy, imaging techniques such as computed tomography (CT), and the invasive gold standard, colonoscopy [6]. Among them, FOBT is non-invasive and cost-effective, making it suitable for large-scale population screening. However, it suffers from limited sensitivity for early-stage lesions and is prone to dietary and medication interference [7]. While CT imaging is also non-invasive, it shows limited sensitivity in detecting small or early-stage lesions [8, 9]. Liquid biopsy, as a minimally invasive technique, analyzes circulating tumor DNA (ctDNA) or miRNAs to monitor tumor-specific genetic alterations in real time. This approach has demonstrated considerable utility in therapeutic response assessment and disease monitoring in advanced CRC. Nonetheless, its clinical application remains constrained by limitations such as reduced sensitivity for early-stage disease, and potential false-negative results due to insufficient ctDNA and miRNAs release or tumor heterogeneity [10, 11]. Colonoscopy is considered the gold standard for CRC diagnosis, enabling direct morphological evaluation of the entire colon, identification of polyps or tumors, and concurrent biopsy or resection. However, its invasive nature, requirement for bowel preparation, risk of perforation, and poor patient compliance restrict its broad applicability in population-wide screening programs [12, 13]. Despite the diverse advantages of current CRC screening methods, limitations in sensitivity, specificity, and accessibility continue to impede their large-scale implementation for early clinical diagnosis.

Radiolabeled molecular probes have been widely applied in tumor diagnosis and therapy, offering capabilities for early tumor detection, precise molecular subtyping, therapeutic response evaluation, and guidance of personalized treatment strategies [14–16]. Several peptide-based diagnostic agents targeting molecular markers such as carcinoembryonic antigen (CEA), human epidermal growth factor receptor 2 (HER2), and fibroblast activation protein (FAP) have already entered clinical trials [17, 18]. In the context of CRC diagnosis, multiple radiolabeled probes have been developed for use in positron emission tomography/computed tomography (PET/CT) and single-photon emission computed tomography/computed tomography (SPECT/CT). For instance, Maleki et al. designed a SPECT/CT probe, ^{99m}Tc-HYNIC-EPPT, targeting the cell surface antigen mucin1 (MUC1), which effectively distinguished CRC tissues from normal tissues. Similarly, Liu et al. developed a PET tracer, ^{68}Ga-DOTA-LS7, targeting CD133, which enabled non-invasive detection of colorectal tumors [19, 20]. While PET/CT offers higher sensitivity, the most commonly used imaging agent, ^{18}F-FDG, demonstrates limited efficacy in detecting advanced colorectal adenomas [21]. Xu et al. reported that combining maximum standardized uptake value (SUVmax) from ^{18}F-FDG PET with colonic wall thickening (CWT) could help identify high-risk adenomas; however, the approach is constrained by strict diagnostic criteria, limited patient applicability, and the need for confirmatory colonoscopy [22]. At present, there is no well-established biomarker specifically for high-risk adenomas, highlighting the need to develop radiolabeled molecular probes capable of monitoring adenoma to carcinoma progression for early CRC diagnosis and intervention.

Here, we employed a multi-model approach involving retrospective clinical analysis, proteomics, and cellular assays to identify critical biomarkers involved in adenoma-to-carcinoma transformation. We identified HSPB1 as significantly upregulated during this transition, with strong associations to tumor proliferation, invasiveness, and metastatic potential. Emerging evidence highlights heat shock protein beta-1 (HSPB1)'s multifaceted role in cancer progression. It functions as a transcriptional co-activator in non-small cell lung cancer by interacting with tRNA-derived fragments to remodel histone modifications and drive proliferation pathways [23]. In gastric cancer, HSPB1 acts as a downstream effector of the FYN/TOPK signaling axis, where its phosphorylation enhances stability and promotes metastasis [24]. HSPB1 also regulates cell‑death pathways such as ferroptosis; in breast cancer, it confers chemoresistance by stabilizing nuclear factor kappa-light-chain-enhancer of activated B cells (NF-κB) signaling [25]. These studies collectively underscore HSPB1 as a promising diagnostic and therapeutic target across malignancies. To enable real-time visualization and precise therapeutic targeting of HSPB1, we developed a novel HSPB1-targeted peptide probe based on the high-affinity sequence QLSKWVGRCLNIN. The probe's *in vivo* pharmacokinetics and targeting properties were optimized through conjugation with 4-(p-iodophenyl) butyric acid (IPBA) and polyethylene glycol (PEG). The final construct, ^{177}Lu-DPTP, demonstrated excellent tumor-targeting specificity and favorable pharmacokinetics *in vivo*. High-contrast imaging and selective accumulation of ^{177}Lu-DPTP were observed in multiple animal models bearing HSPB1-overexpressing tumors. SPECT/CT dynamic imaging and biodistribution studies further validated its high-resolution imaging and strong tissue selectivity in both patient-derived xenograft (PDX) and orthotopic low rectal cancer models, achieving tumor to muscle signal ratios exceeding 40-fold. Importantly, ^{177}Lu-DPTP exhibited potent radiotherapeutic efficacy in orthotopic CRC models, inducing dose-dependent tumor suppression and prolonging survival without evident hepatic or renal toxicity or systemic adverse effects, underscoring its favorable biocompatibility and safety profile (Scheme 1). Collectively, this study not only elucidates the biological significance of HSPB1 in CRC tumorigenesis and progression, but also introduces the first HSPB1-targeted radiolabeled peptide probe with dual diagnostic and therapeutic capabilities. The successful preclinical validation of this theranostic agent establishes an integrated platform for "early detection–precise classification–targeted therapy" of colorectal cancer. This strategy provides a novel approach and practical tool for early screening of high-risk adenoma populations and precision radiotherapy, offering substantial potential for clinical translation and widespread application.

2 Results

2.1 Identification of high-risk adenoma subtypes and key molecular alterations during adenoma to carcinoma transition

The adenoma-carcinoma sequence represents one of the principal pathways in CRC development, although the overall malignant transformation rate of colorectal adenomas remains relatively low (approximately 5%). The precise molecular events driving this transformation are not fully understood. To clarify which adenoma subtypes are more prone to malignant progression and to elucidate potential underlying mechanisms, we conducted a retrospective clinical analysis combined with proteomic profiling. Based on

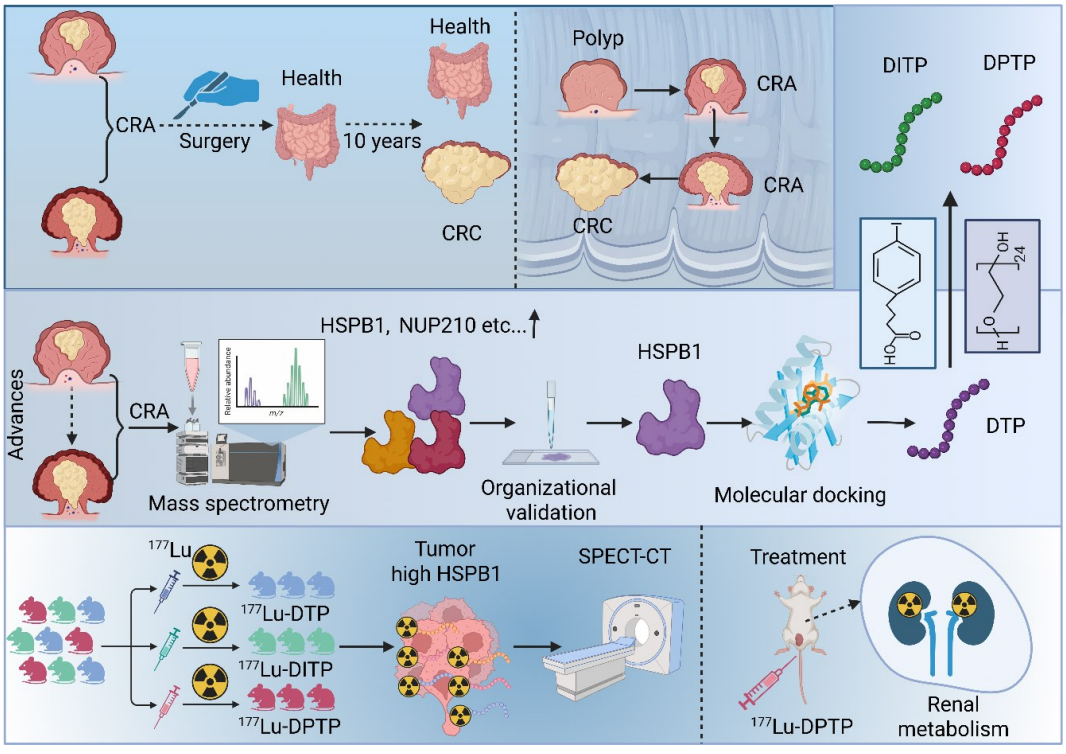

Scheme 1 Schematic diagram of screening for malignant markers of colorectal adenoma to carcinoma transformation and development of nuclear drug diagnosis and treatment, created with BioRender.

histological characteristics, we selected four representative subtypes of colorectal adenomas: tubular adenoma, villous tubular adenoma, tubular villous adenoma, and villous adenoma (Fig. 1(a), and Fig. S1 in the Electronic Supplementary Material (ESM)). Microscopically, tubular adenoma is characterized by predominantly tubular glands arranged in a crowded, branching, and back-to-back pattern. The glandular contours are generally regular or mildly irregular, with a villous component comprising < 25% of the lesion. In contrast, villous adenoma consists almost entirely of villous structures, exhibiting numerous elongated finger-like or leaf-like projections with prominent fibrovascular cores. The villous structures are diffusely and densely arranged, accounting for > 75% of the lesion. The overlying epithelium often demonstrates more marked adenomatous dysplasia. Both tubular-villous adenoma and villous-tubular adenoma represent mixed forms, in which tubular and villous structures are present as significant components. Specifically, tubular-villous adenoma contains a villous component ranging from 25% to 50%, whereas villous-tubular adenoma contains a villous component ranging from 50% to 75%. The overlying epithelium in these mixed forms generally exhibits dysplasia. We retrospectively analyzed clinical data from 4123 patients diagnosed with colorectal adenomas at the First Affiliated Hospital of Soochow University between 2008 and 2018 and performed long-term follow-up. The overall malignant transformation rate was 3.8%. Specifically, the transformation rates were 0.913% (21/2300) for tubular adenomas, 4.1% (53/1298) for villous-tubular adenomas, 9.5% (24/252) for tubular villous adenoma, and 21.2% (58/273) for villous adenomas. Chi-square analysis revealed statistically significant differences in CRC transformation rates between villous adenoma and tubular adenoma, tubular villous adenoma and tubular adenoma, and villous adenoma and tubular villous adenoma (Table S2 in the ESM). Further analysis showed that patients aged > 65 years had a significant higher risk of CRC development compared to those aged ≤ 65 years (Table S3 in the ESM). Within the tubular adenoma group, age > 65 years was also significantly associated with increased CRC risk (P = 0.038). However, in the other three subtypes, no significant correlations were observed between malignant progression and variables such as age, sex, lesion location, or size (Tables S4–S6 in the ESM). Additionally, in villous adenomas, rectal lesions were more likely to progress to CRC (Table S7 in the ESM).

To explore the molecular features of malignant transformation, we selected tissue samples from three pairs of adenoma patients who did or did not develop CRC over 10 years of follow-up and performed proteomic analysis. Label-free quantitative mass spectrometry (LC-MS/MS) was used to analyze adenoma tissue samples, identifying 6054 proteins in total, with 4404 quantified. Proteins with a quantitative ratio (progression vs. control, P/C) greater than 1.5 were considered upregulated, and those with a ratio less than 1/1.5 were considered downregulated. In total, 28 proteins were significantly upregulated and 33 downregulated (Table S8 in the ESM). Further screening identified 78 differentially expressed proteins meeting the threshold (|Fold change| > 1.4, P < 0.05), including 36 upregulated and 42 downregulated proteins. A volcano plot illustrated the top four upregulated and downregulated proteins with the greatest fold change (Fig. 1(b)), and a heatmap showed the overall distribution of differential expression (Fig. 1(c)). These proteins were analyzed using the Search Tool for the Retrieval of Interacting Genes/Proteins (STRING) database, and protein–protein interaction (PPI) networks were constructed using Cytoscape with the MCODE plugin, revealing a highly connected module containing 43 core proteins (Fig. 1(d)). Notably, HSPB1, aconitase 2 (ACO2), STIP1 homology and u-box containing

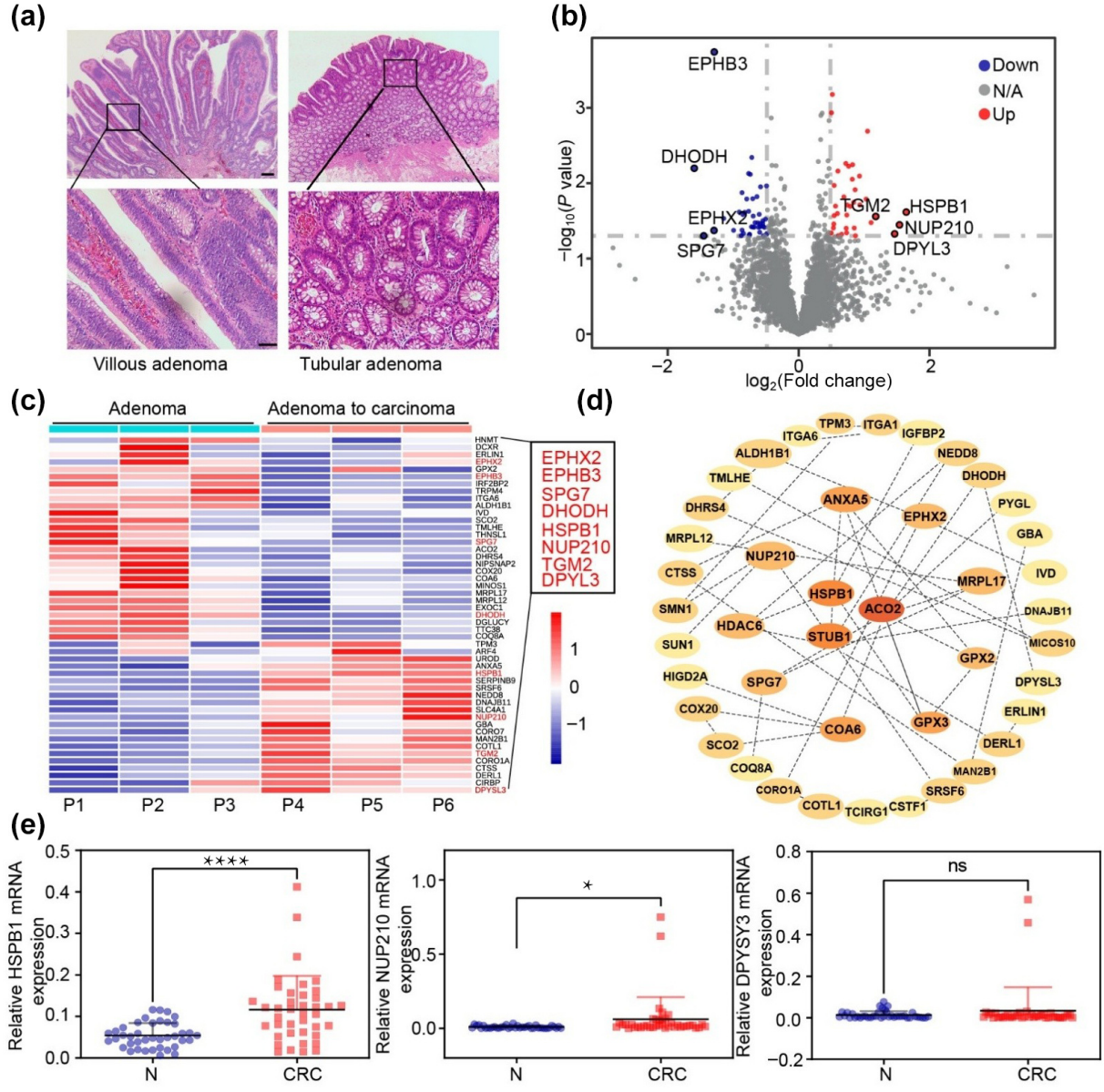

Figure 1 Molecular characterization of high risk adenoma subtypes and adenoma-carcinoma transformation in colorectal adenomas. (a) Representative hematoxylin and eosin (H&E) staining images of villous and tubular adenomas in colorectal tissues. Scale bars: 100 μm. (b) Quantitative volcano plot displaying differentially expressed proteins between high-risk and low-risk adenomas. Upregulated and downregulated proteins are highlighted. (c) Heatmap showing the relative expression levels of significantly altered proteins across different patient samples. (d) Protein–protein interaction network of differentially expressed proteins. Node color intensity indicates the degree of connectivity (darker color represents higher degree). (e) qRT-PCR analysis of *HSPB1*, *NUP210*, and *DPYSL3* mRNA expression in 40 paired CRC tissue samples (n = 40). Data are presented as mean ± standard deviation (SD) (n = 40). Statistical significance between paired tumor and adjacent normal tissues was determined by a paired two-tailed Student's t-test. ns: not significant; $^{*}P < 0.05$; $^{****}P < 0.001$.

protein 1 (STUB1), and nucleoporin 210 (NUP210) were positioned at the center of this network. To validate differential expression, we selected eight genes with the most pronounced changes for quantitative reverse transcription polymerase chain reaction (qRT-PCR) analysis in 40 paired CRC and adjacent normal tissues. Among them, HSPB1 and NUP210 were consistently upregulated in tumor samples, with HSPB1 showing the most significant increase (Fig. 1(e) and Fig. S2 in the ESM). HSPB1, a small heat shock protein, plays a key role in cellular stress responses and has been implicated in the pathogenesis of various cancers. In colorectal cancer, HSPB1 is involved in tumor proliferation, metastasis, and therapeutic resistance [26, 27]. These findings suggest that HSPB1 may not only participate in the adenoma-to-carcinoma transition but also contribute to CRC progression, underscoring its potential as an early diagnostic biomarker and therapeutic target.

2.2 Validation of HSPB1 expression during adenoma to carcinoma progression at the protein level

To verify the protein level expression changes of HSPB1 during the adenoma-to-carcinoma transition, we performed immunohistochemical (IHC) staining on tissue samples from 10 pairs of adenoma patients who either progressed to carcinoma or remained benign during follow-up. The results demonstrated a statistically

significant difference in HSPB1 IHC scores between adenomas that underwent malignant transformation and those that did not (Fig. 2(a)). Consistent with previous literature, comparative analysis of five pairs of progressive rectal cancer tissues and their adjacent non-tumorous counterparts revealed a marked increase in HSPB1 expression in the tumor tissues (Fig. 2(b)). To further substantiate these findings, we systematically assessed HSPB1 expression in a cohort of 20 tissue samples representing tubular adenoma, villous-tubular adenoma, villous adenoma, and CRC. IHC analysis revealed significantly elevated HSPB1 expression in CRC tissues compared to adenoma tissues, with the difference in IHC scores reaching statistical significance (Fig. 2(c)). These results suggest that HSPB1 expression may increase progressively during CRC development and may serve as a potential biomarker to predict malignant transformation of colorectal adenomas.

2.3 HSPB1 promotes proliferation, invasion, and migration of colorectal cancer cells

Building upon the tissue level validation, we next investigated the functional role of HSPB1 expression in colorectal cancer cells. First, we examined the expression levels of HSPB1 across a panel of CRC cell lines, including DLD1, HCT116, HT29, HCT8, LoVo, RKO, SW480, and SW620. The results showed that both mRNA and protein levels of HSPB1 were markedly lower in HT29 and SW620 cells compared to the other cell lines (Figs. 3(a) and 3(b)). To explore the potential role of HSPB1 in CRC metastasis, we ectopically overexpressed HSPB1 in HT29 and SW620 cells using a lentiviral system. The efficiency of transfection was confirmed by Western blot analysis (Fig. 3(c)). Subsequently, cell counting kit-8 (CCK-8) assays were conducted to evaluate the impact of HSPB1 on cell proliferation. The results indicated that HSPB1 overexpression significantly enhanced the clonogenic capacity of both cell lines, suggesting a stimulatory effect on proliferation (Fig. 3(d)). In addition, to assess the effects of HSPB1 on cellular migration and invasion, we performed Transwell migration and Matrigel invasion assays in the HSPB1 overexpressed cells. The data demonstrated that HSPB1 overexpression substantially increased the migratory and invasive capabilities of HT29 and SW620 cells (Fig. 3(e)). Collectively, these results indicate that HSPB1 acts as a positive regulator of proliferation, migration, and invasion in colorectal cancer cells. These findings suggest that HSPB1 may not only contribute to the adenoma-to-carcinoma transition but also play a critical role in CRC progression. Early and rapid detection of

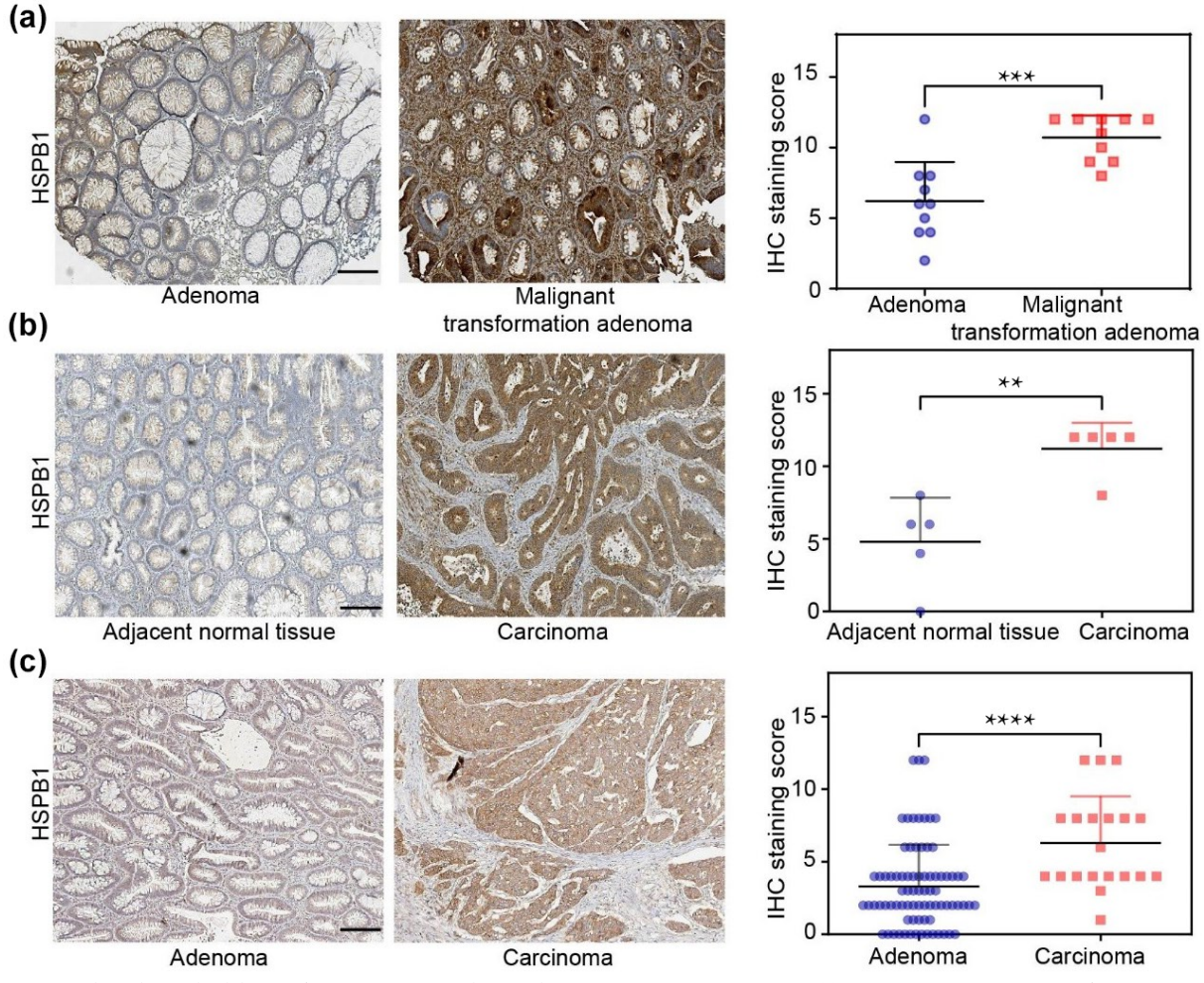

Figure 2 Immunohistochemical validation of HSPB1 expression during adenoma to carcinoma progression. (a) Representative IHC staining of HSPB1 in 10 pairs of colorectal adenoma tissues with and without malignant transformation. IHC scores are shown on the right. (b) IHC staining of HSPB1 in 5 pairs of progressive colorectal cancer tissues and corresponding adjacent non-tumor tissues. IHC scores are shown on the right. (c) Comparative analysis of HSPB1 expression in various stages of adenoma and CRC. IHC scores are shown on the right. Scale bars: 100 μm. Statistical significance between paired tumor and adjacent normal tissues was determined by a paired (in panel (b)) or unpaired (in panels (a) and (c)) two-tailed Student's t-test. ns: not significant; $^{*}P < 0.05$; $^{***}P < 0.001$, $^{****}P < 0.0001$.

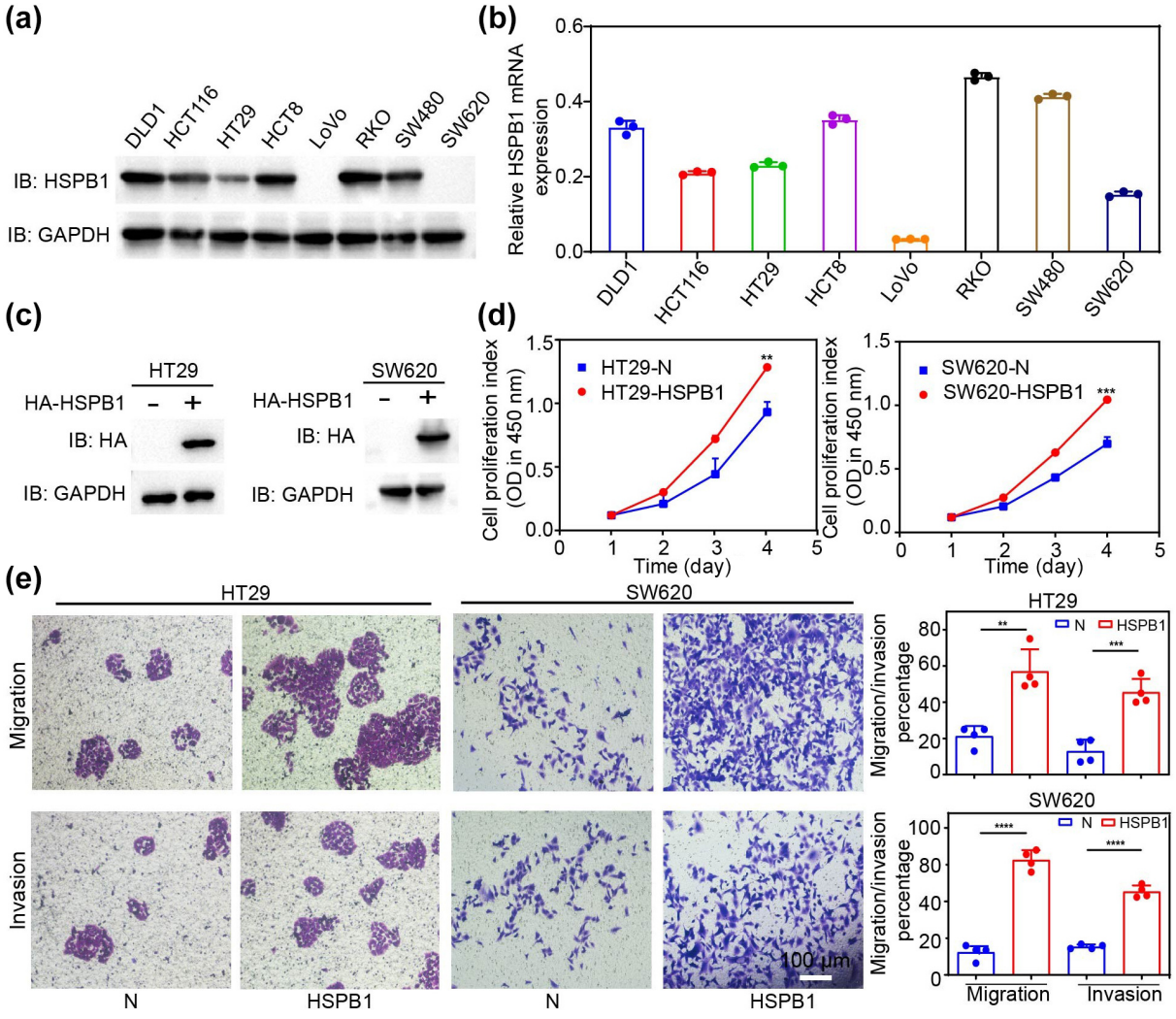

Figure 3 Functional validation of HSPB1 in CRC cell lines. (a) Western blot analysis of HSPB1 protein in a panel of human CRC cell lines (DLD1, HCT116, HT29, HCT8, LoVo, RKO, SW480, and SW620). (b) Quantitative real-time PCR analysis of HSPB1 mRNA expression across the same CRC cell line. (c) Western blot validation of stable HSPB1 overexpression in HT29 and SW620 cells following lentiviral transduction. (d) CCK-8 assays demonstrating that HSPB1 overexpression significantly enhances cell proliferation and clonogenic potential in both HT29 and SW620 cells (n = 3). (e) Transwell migration and Matrigel invasion assays showing increased migratory and invasive capacities upon HSPB1 overexpression in HT29 and SW620 cells (n = 4). Data are expressed as mean ± SD. Statistical analysis was performed using an unpaired two-tailed Student's t-test. $^{*}P < 0.05$; $^{***}P < 0.001$, $^{****}P < 0.0001$.

HSPB1 expression could thus provide valuable insights for early screening and intervention in colorectal cancer.

2.4 Design of radiolabeled probes targeting HSPB1

Radiolabeled protein or peptide-based probes offer distinct advantages in molecular imaging and cancer therapy. Their design flexibility allows for bio-conjugation with various radionuclides to achieve specific targeting of molecular markers [28]. Previous studies have identified 25 peptide sequences capable of binding to HSPB1 using yeast two-hybrid screening, among which the P11 sequence demonstrated the highest affinity [29]. Building upon this, we employed molecular dynamics (MD) simulations combined with molecular mechanics with generalized born and surface area (MM-GBSA) calculations to estimate the binding free energy of these peptides with HSPB1. To further optimize peptide binding, we applied the Amber thermodynamic integration (TI) method to predict beneficial mutations at key residues. Mutations were introduced at positions S3, G4, and W5, generating six candidate sequences with significantly enhanced binding energies. Molecular docking was performed using the Start GRAMM program, and the PDBePISA platform was used to calculate binding interfaces and affinity parameters. Among all sequences tested, QLSKWVGRCLNIN exhibited the strongest binding energy with HSPB1, reaching −11.6 kcal/mol, outperforming P11 and other candidates. The peptide showed excellent spatial complementarity within the HSPB1 binding pocket and maintained stable binding under physiological conditions (Figs. 4(a) and 4(b), Fig. S3 in the ESM). Based on this sequence, we designed a novel HSPB1-targeting molecular probe. To enhance cellular uptake, a cell-penetrating peptide (RKKRRQRRR, known as TAT) was fused to the N-terminus of QLSKWVGRCLNIN, followed by DOTA (1,4,7,10-tetraazacyclododecane-1,4,7,10-tetraacetic acid) conjugation for radiolabeling, yielding DOTA-TAT-QLSKWVGRCLNIN (DTP). Subsequent molecular docking indicated that the TAT modified peptide maintained high affinity for HSPB1, with a binding energy of −11.9 kcal/mol (Fig. S4 in the ESM), suggesting that the addition of the TAT sequence did not compromise binding efficiency.

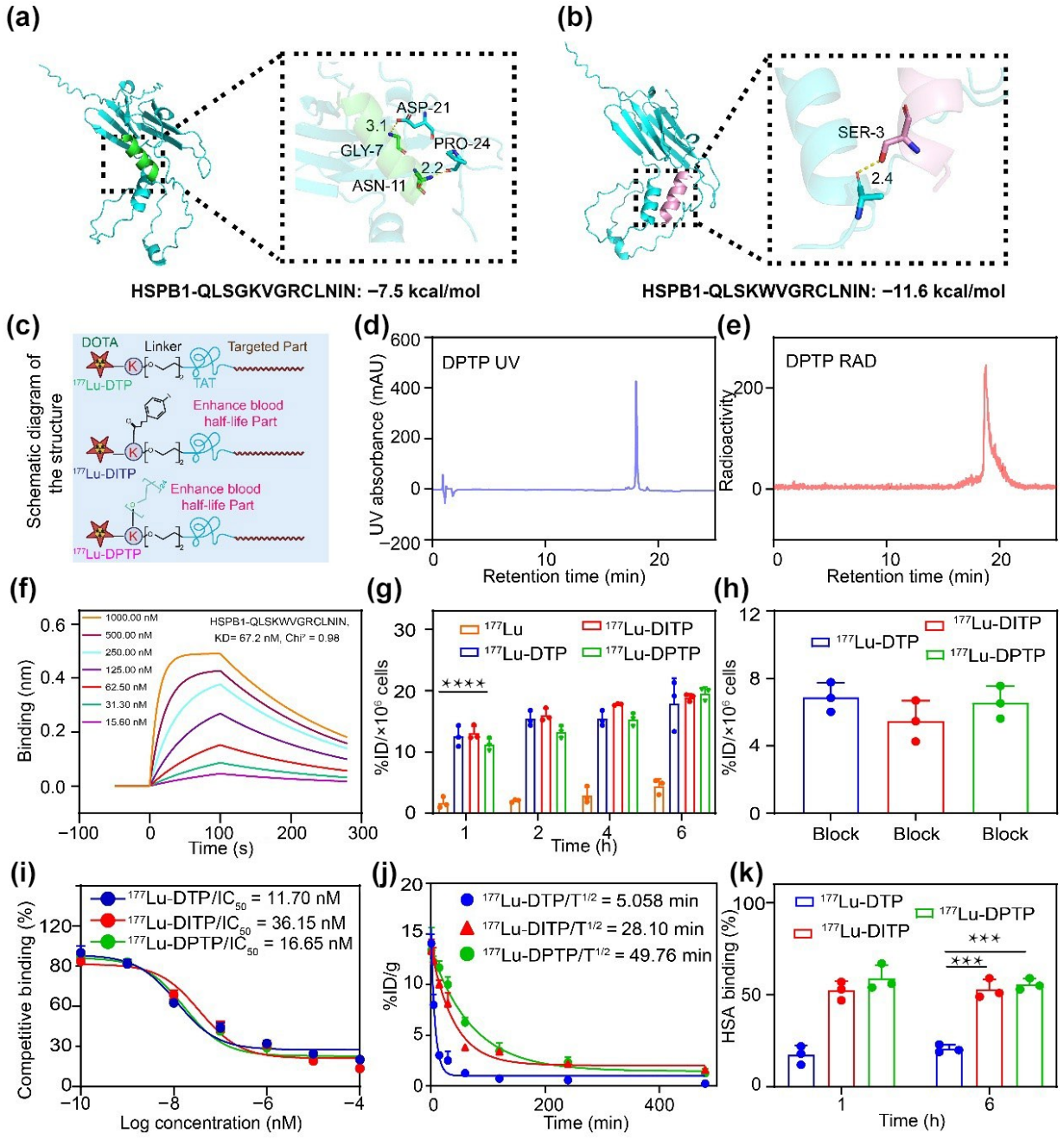

Figure 4 Design, synthesis, and *in vitro* evaluation of HSPB1-targeted radiolabeled peptide probes. Molecular docking analysis of peptide ligands (a) QLSGKVGRCLNIN and (b) QLSKWVGRCLNIN with HSPB1. (c) Schematic representation of the chemical structures of DTP, DITP, and DPTP, showing the sequential incorporation of 4-(p-iodophenyl) butyric acid and PEG_{24} modifications to optimize pharmacokinetics detailed sequences are available in the ESM. (d) HPLC profiles showing UV absorption and (e) radiochemical purity of ^{177}Lu-labeled DTP derivatives. (f) Biolayer interferometry (BLI) sensograms showing the real-time binding response of the QLSKWVGRCLNIN peptide to immobilized HSPB1 at the indicated concentrations. The KD was calculated to be 67.2 nM. (g) Cellular uptake of free ^{177}Lu versus, ^{177}Lu-DTP, ^{177}Lu-DITP, and ^{177}Lu-DPTP in CT26-HSPB1 cells at different incubation times. (h) Competitive binding assays showing reduced uptake of ^{177}Lu-DTP, ^{177}Lu-DITP and ^{177}Lu-DPTP in the presence of 2000-fold excess unlabeled peptide, confirming specific binding to HSPB1. (i) Dose–response curves from competition assays for ^{177}Lu-DTP, ^{177}Lu-DITP, and ^{177}Lu-DPTP in CT26-HSPB1 cells, with calculated IC_{50} values of 11.70, 36.15, and 16.65 nM, respectively. (j) Pharmacokinetic analysis in healthy mice demonstrating blood half-lives ($T_{1/2}$) of each probe. (k) Evaluation of plasma protein binding by incubating human serum albumin (HSA) with each probe. Data are presented as mean ± SD from three independent experiments. Statistical analysis was performed using t-tests. $^{***}P < 0.001$, $^{****}P < 0.0001$.

A major challenge of radiolabeled peptide probes is their rapid blood clearance. To improve pharmacokinetics and *in vivo* stability, we incorporated two modifications known to enhance plasma protein binding and circulation time: 4-(p-iodophenyl) butyric acid and PEGylation [30, 31]. These modifications yielded two derivative peptides: DOTA-IP-TAT-QLSKWVGRCLNIN (DITP) and DOTA-PEG_{24}-TAT-QLSKWVGRCLNIN (DPTP) (Fig. 4(c)). Radiolabeling efficiency of DTP, DITP, and DPTP with ^{177}Lu was evaluated. HPLC analysis showed a single radiolabeled peak between 0.2 and 2 min under ultraviolet (UV) detection, with radiochemical yields exceeding 98% for all three peptides (Figs. 4(d) and 4(e), and Fig. S5 in the ESM). Stability assays demonstrated that

the ^{177}Lu-labeled peptides retained more than 90% of their radioactivity after 48 h in phosphate-buffered saline (PBS) and 10% fetal bovine serum (Fig. S6 in the ESM). To biochemically validate the direct and specific interaction between the optimized peptide QLSKWVGRCLNIN and HSPB1, we performed biolayer interferometry (BLI). Recombinant human HSPB1 protein was immobilized on the biosensor, and the association and dissociation kinetics of the peptide were measured at varying concentrations. The data fitted well to a 1:1 binding model, yielding an equilibrium dissociation constant (KD) of 67.2 nM (Fig. 4(f)). This result provides direct quantitative evidence of a high-affinity interaction, confirming that the designed peptide specifically binds to HSPB1. Together with the computational docking analysis, this biochemical validation firmly establishes QLSKWVGRCLNIN as a suitable targeting moiety for HSPB1 (Fig. 4(f)). Furthermore, we constructed a CT26 cell line stably overexpressing HSPB1 (CT26-HSPB1) via lentiviral transduction. Successful expression was confirmed by Western blot (Figs. S7 and S8 in the ESM). Confocal microscopy revealed enhanced intracellular uptake of Cy5.5-labeled DTP in CT26-HSPB1 cells compared to controls, with significant accumulation observed after 2 h of incubation (Fig. S9 in the ESM). Further uptake experiments demonstrated that when incubated with ^{177}Lu-DTP, ^{177}Lu-DITP, or ^{177}Lu-DPTP, CT26-HSPB1 cells exhibited uptake rates exceeding 18%, significantly higher than cells incubated with free ^{177}Lu (Fig. 4(g)). Competitive inhibition assays confirmed target specificity: a 2000-fold excess of unlabeled peptide reduced uptake of all three radiolabeled peptides to below 8% (Fig. 4(h)), indicating that cellular uptake was largely dependent on specific HSPB1 binding. To quantitatively evaluate binding affinity, competition binding assays were performed using graded concentrations (10^{-10} to 10^{-5} M) of unlabeled peptides and 0.74 MBq of ^{177}Lu-DTP co-incubated with CT26-HSPB1 cells for 6 h. Gamma counting followed by non-linear regression analysis yielded IC_{50} values of 11.70, 36.15, and 16.65 nM for ^{177}Lu-DTP, ^{177}Lu-DITP, and ^{177}Lu-DPTP, respectively (Fig. 4(i)). Among them, DTP exhibited the highest binding affinity. To assess biocompatibility, CT26-HSPB1 cells were incubated with unlabeled DTP at a concentration of 400 nM. Cell viability remained high, indicating favorable biosafety (Fig. S10 in the ESM). In cytotoxicity assays, ^{177}Lu-DTP showed significantly enhanced dose-dependent tumoricidal effects compared to free ^{177}Lu (Fig. S11 in the ESM). Pharmacokinetic profiles were further evaluated in healthy mice. The blood half-life ($T_{1/2}$) of ^{177}Lu-DTP was 5.058 min, while ^{177}Lu-DITP and ^{177}Lu-DPTP exhibited prolonged half-lives of 28.10 and 49.76 min, respectively (Fig. 4(j)). Human serum albumin (HSA) binding assays revealed that DTP exhibited a low binding rate (~ 10%) after 6 h of incubation, whereas DITP and DPTP achieved binding rates of approximately 60% (Fig. 4(k)), consistent with improved pharmacokinetic behavior. These data collectively indicate that 4-(p-iodophenyl) butyric acid and PEG modification can significantly enhance plasma protein binding and prolong circulation time. Based on these findings, ^{177}Lu-DITP and ^{177}Lu-DPTP, which exhibited superior pharmacokinetic profiles, were selected for subsequent *in vivo* studies. In summary, we successfully developed a class of HSPB1-targeted peptide probes with high binding specificity and favorable stability, enabling precise monitoring of HSPB1 expression for potential applications in colorectal cancer imaging and therapy.

2.5 Imaging and therapeutic evaluation of ^{177}Lu-DITP and ^{177}Lu-DPTP targeting HSPB1

To further characterize the *in vivo* profile of ^{177}Lu-DTP, we performed a quantitative biodistribution study in CT26-HSPB1 tumor-bearing mice at 2, 4, 8, and 24 h post-injection. ^{177}Lu-DTP showed specific, time-dependent accumulation in tumors, with peak uptake at 4 h (3.8% ± 0.3% inhibitory dose (ID)/g), followed by gradual clearance (Fig. S12 in the ESM). Non-target organ uptake remained low, consistent with its favorable targeting selectivity and rapid renal clearance. The observed decline in tumor uptake after 8 h may be related to the relatively short blood half-life of the unmodified peptide scaffold. Given the relatively short blood half-life of DTP, we selected ^{177}Lu-DITP and ^{177}Lu-DPTP which exhibit superior pharmacokinetic properties for subsequent theranostic validation using subcutaneous xenograft tumor models (Fig. 5(a)). In mice bearing dual tumors of HT29 (control) and HT29-HSPB1 (overexpressing), dynamic SPECT/CT imaging was performed after intravenous administration of ^{177}Lu-DPTP (14.8 MBq per mouse). Radiotracer uptake was observed as early as 2 h post-injection in the HSPB1 positive tumor on the right flank, while the control tumor on the left exhibited minimal signal. Tumor uptake plateaued at 4 h, showing a high tumor to background contrast over time (Fig. 5(b)). To confirm targeting specificity, a blocking study was conducted by pre-injecting excess unlabeled DPTP (2 mmol) one hour prior to radiotracer administration. In the blocked group, radioactivity accumulation in the HT29-HSPB1 tumors was significantly reduced, with attenuated signals at 24 h post-injection, confirming the specific binding of ^{177}Lu-DPTP to HSPB1. Biodistribution data further revealed that ^{177}Lu-DPTP was predominantly cleared via renal excretion while showing selective retention in HSPB1 overexpressed tumors (Fig. 5(c)). Following successful validation in the HT29 model, we evaluated ^{177}Lu-DPTP targeting performance in the CT26 model. Mice bearing CT26 (HSPB1-negative) and CT26-HSPB1 tumors received intravenous injections of ^{177}Lu-DPTP (14.8 MBq per mouse). Dynamic SPECT/CT imaging showed minimal uptake in CT26 tumors, comparable to normal tissue, while CT26-HSPB1 tumors exhibited specific radiotracer accumulation beginning at 4 h and excellent tumor to background contrast by 8 h. No significant radioactivity retention was observed in non-tumor tissues except the kidneys (Fig. 5(d)). Blocking experiments further confirmed specificity; pre-injection of unlabeled DPTP markedly reduced ^{177}Lu-DPTP uptake in CT26-HSPB1 tumors without altering distribution in normal tissues (Fig. 5(e)). Quantitative biodistribution analysis (3.7 MBq per mouse) revealed time-dependent uptake in CT26-HSPB1 tumors, with values of 2.56 ± 0.3, 2.98 ± 0.2, 4.12 ± 0.2, and 5.9 ± 0.4 %ID/g at 2, 4, 8, and 24 h, respectively. Uptake in tumor tissue was significantly higher than in other organs (excluding kidneys), and the tumor to muscle ratio reached up to 40 ± 15 (Fig. 5(f) and Fig. S13(a) in the ESM). These results confirmed that ^{177}Lu-DPTP accumulation was specifically mediated by HSPB1 expression and primarily cleared through renal pathways. We next evaluated the targeting capability of ^{177}Lu-DITP. In the dual CT26/CT26-HSPB1 tumor model, mice received intravenous injections of ^{177}Lu-DITP (14.8 MBq per mouse). SPECT/CT imaging showed no discernible signal in CT26 tumors, while CT26-HSPB1 tumors exhibited clear radiotracer uptake beginning at 4 h and reaching a stable distribution by 8 h, with high tumor to background contrast (Fig. 5(g)). Notably, significant liver accumulation was observed, likely due to uptake by the

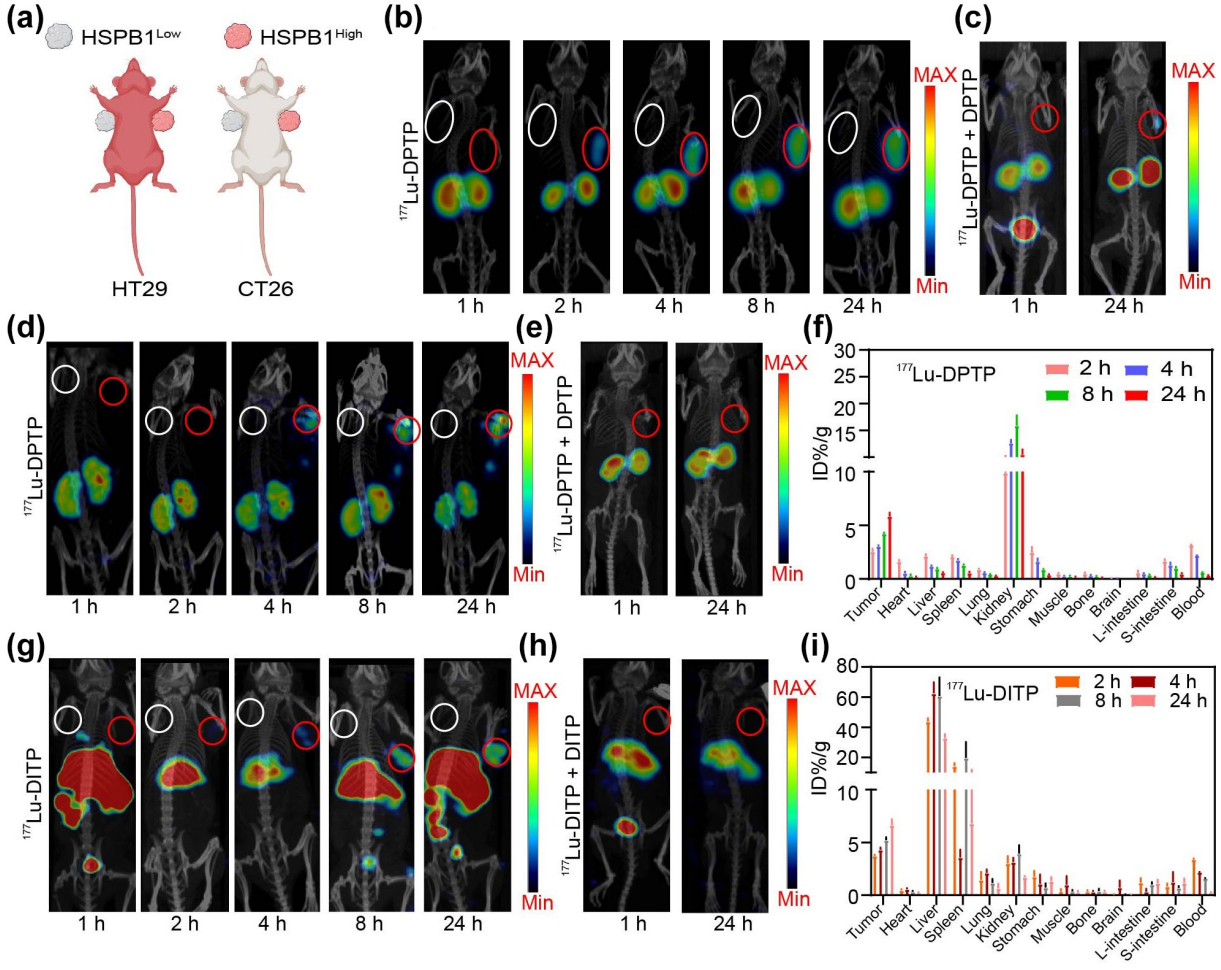

Figure 5 SPECT/CT imaging and biodistribution analysis of ^{177}Lu-labeled HSPB1-targeting peptide probes in subcutaneous tumor models. (a) Schematic illustration of a bilateral subcutaneous tumor mouse model with differential HSPB1 expression: high on the right (side) (HSPB1^{+} tumor) and low on the left (side) (control tumor). (b) SPECT/CT images of mouse with HT29-N (R) and HT29-HSPB1 (L) tumors at various time points after i.v. injection of ^{177}Lu-DPTP (14.8 MBq per mouse). (c) Blocking experiments showing diminished uptake of ^{177}Lu-DPTP in HT29-HSPB1 tumors after pre-injection of excess unlabeled DPTP, confirming binding specificity. (d) SPECT/CT images of mouse with CT26-N (R) and CT26-HSPB1 (L) tumors at various time points after i.v. injection of ^{177}Lu-DPTP (14.8 MBq per mouse). (e) Blocking experiments with unlabeled DPTP significantly reduced probe uptake in CT26-HSPB1 tumors without affecting distribution in normal tissues. (f) Analysis of the biodistribution of ^{177}Lu-DPTP in the mice. (g) SPECT/CT images of mouse with CT26-N (R) and CT26-HSPB1 (L) tumors at various time points after i.v. injection of ^{177}Lu-DITP (14.8 MBq per mouse). (h) Blocking experiments demonstrating that pre-treatment with excess unlabeled DITP significantly suppressed ^{177}Lu-DITP uptake in CT26-HSPB1 tumors. (i) Analysis of the biodistribution of ^{177}Lu-DITP in the mice. Data are presented as mean ± SD from three independent experiments (n = 3).

reticuloendothelial system (RES) [32]. Blocking studies demonstrated that pre-injection of unlabeled DITP significantly reduced tumor uptake of ^{177}Lu-DITP in CT26-HSPB1 tumors, reinforcing HSPB1-mediated specificity (Fig. 5(h)). Biodistribution data confirmed time-dependent uptake in CT26-HSPB1 tumors, with uptake values of 3.6 ± 0.1, 4.2 ± 0.2, 5.15 ± 0.2, and 6.5 ± 0.5 %ID/g at 2, 4, 8, and 24 h, respectively (Fig. 5(i)). The tumor to muscle ratio reached 15 ± 5 (Fig. S13(b) in the ESM). However, liver uptake was as high as 40–60 %ID/g, raising concerns regarding potential hepatic radiation toxicity. Uptake in other organs, including the skeleton, remained lower than in HSPB1 overexpressed tumors. These findings suggest that although ^{177}Lu-DITP exhibits promising tumor-targeting capability, its significant hepatic retention may limit its clinical applicability. PEGylation is a well-established strategy for improving the pharmacokinetics of radiopharmaceuticals by enhancing solubility and prolonging circulation time. This modification also reduces non-specific uptake by the RES. In comparison to ^{177}Lu-DITP, the PEGylated variant ^{177}Lu-DPTP exhibited comparable HSPB1-specific tumor targeting along with improved pharmacokinetic behavior. Based on these collective results, we selected ^{177}Lu-DPTP for subsequent *in vivo* therapeutic studies. This probe demonstrated the ability to selectively bind HSPB1 and accurately visualize its expression in tumor tissues.

2.6 Imaging and therapeutic evaluation of ^{177}Lu-DPTP in PDX and low rectal cancer models

PDX models preserve the histological architecture, molecular heterogeneity, and therapeutic response profiles of primary tumors and have become a crucial bridge between basic research and clinical applications [33, 34]. We investigated whether ^{177}Lu-DPTP could be used to detect endogenous HSPB1 expression as an indicator of disease status in early stage CRC. Tumor tissues with early malignant features were selected from surgical samples of CRC patients, sectioned into small fragments, and subcutaneously implanted into nude mice to establish PDX models. Stable and reproducible CRC-PDX models were obtained through serial

passaging. To evaluate the *in vivo* behavior of ^{177}Lu-DPTP, mice bearing CRC-PDX tumors received intravenous injections of ^{177}Lu-DPTP (14.8 MBq per mouse), followed by SPECT/CT imaging at 1, 2, 4, 8 and 24 h post-injection. The results showed clear radiotracer accumulation at the tumor site beginning at 2 h, peaking at 4 h, and remaining stable thereafter. Apart from renal clearance, no significant uptake was observed in normal tissues (Fig. 6(a)). These findings indicate that ^{177}Lu-DPTP enables effective imaging of early-stage CRC lesions and provides direct visual support for early diagnosis. We further assessed the therapeutic potential of ^{177}Lu-DPTP in a low rectal cancer model. Given the clinical importance of anus-preserving treatment in low rectal cancer (typically defined as tumors located ≤ 5 cm from the anal verge), early intervention with radiolabeled targeted therapy offers the potential to both control tumor progression and preserve anal function, significantly improving patient quality of life. CT26-HSPB1 tumor cells were orthotopically implanted into the distal rectum of BALB/c mice to establish the model. Due to uncertainty in urinary excretion, direct SPECT/CT imaging of the rectal region could be affected by non-specific signals. To avoid this, 24 h post-injection of ^{177}Lu-DPTP (14.8 MBq per mouse), *ex vivo* SPECT/CT imaging was performed on harvested heart, liver, spleen, lung, kidney, and tumor tissues. The images revealed a high tumor to background contrast (Fig. 6(b)). Quantitative biodistribution analysis further confirmed that ^{177}Lu-DPTP accumulated in the orthotopic rectal tumor with an uptake of approximately 5 ± 0.6 %ID/g (Fig. 6(c)), demonstrating effective localization of the probe at the low rectal tumor site. To definitively ascertain whether the therapeutic efficacy required the covalent conjugation of the radionuclide to the targeting peptide, an additional control group was evaluated. Mice bearing CT26-HSPB1 tumors were treated with a physical mixture of non-radiolabeled DPTP and free ^{177}Lu (Group G6), administered at the same peptide (5 nmol) and radioactivity (14.8 MBq) doses as the high-dose ^{177}Lu-DPTP group (G5). Notably, the physical

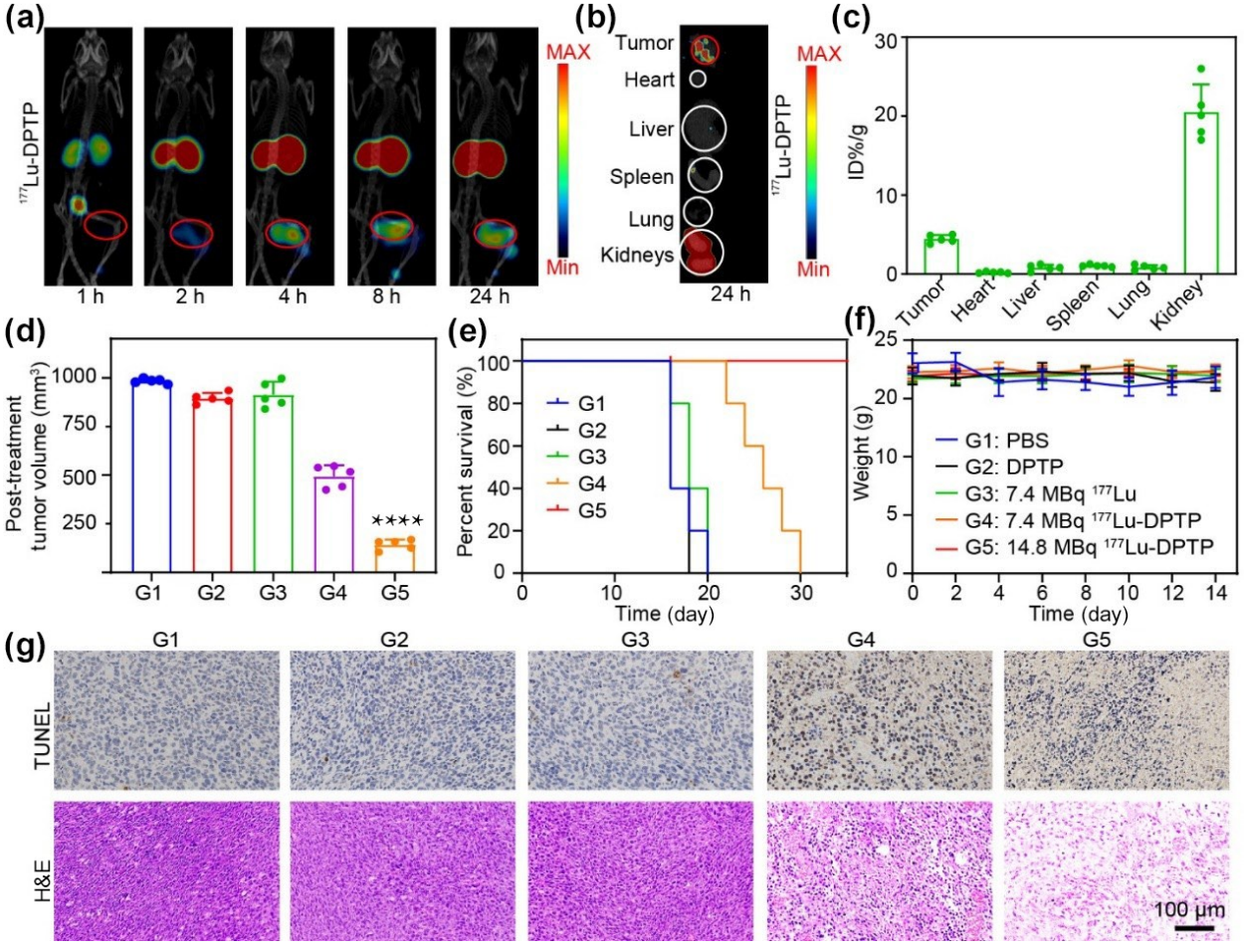

Figure 6 SPECT/CT imaging and therapeutic evaluation of ^{177}Lu-DPTP in PDX and orthotopic low rectal cancer models. (a) SPECT/CT images of a colorectal cancer PDX model with high endogenous HSPB1 expression at 1, 2, 4, 8, and 24 h after intravenous injection of ^{177}Lu-DPTP (14.8 MBq per mouse), showing progressive and tumor-specific accumulation with minimal off-target distribution. (b) SPECT/CT imaging of major organs (heart, liver, spleen, lungs, kidneys) at 24 h post-injection of ^{177}Lu-DPTP in a CT26-HSPB1 orthotopic low rectal tumor model, confirming high tumor-to-background signal. (c) Biodistribution analysis of ^{177}Lu-DPTP in the orthotopic rectal tumor model, showing specific accumulation in tumor tissue. Data are presented as mean ± SD (n = 5). (d) Tumor growth curves of CT26-HSPB1-bearing mice treated with PBS (G1), DPTP (20 nM, G2), free ^{177}Lu (14.8 MBq, G3), ^{177}Lu-DPTP (7.4 MBq, G4), and ^{177}Lu-DPTP (14.8 MBq, G5), showing dose-dependent tumor suppression over 14 days. (e) Kaplan–Meier survival analysis demonstrating improved survival in ^{177}Lu-DPTP-treated groups, particularly at 14.8 MBq dose. (f) Body weights monitoring across treatment groups show no significant fluctuations, suggesting minimal systemic toxicity. (g) Representative histological sections of tumor tissues stained with H&E and terminal deoxynucleotidyl transferase dUTP nick-end labeling (TUNEL), revealing extensive cell damage and apoptosis in tumors from the ^{177}Lu-DPTP (14.8 MBq) treatment group. Data are presented as mean ± SD from five independent experiments, statistical significance was determined by an unpaired two-tailed Student's t-test. $^{****}P < 0.0001$.

mixture (G6) failed to inhibit tumor growth, with kinetics similar to the PBS control (G1), whereas the covalently conjugated ^{177}Lu-DPTP (G5) remained highly effective (Fig. S14 in the ESM). This result conclusively demonstrates that the observed antitumor effect is not attributable to nonspecific co-localization or synergy between separately administered components but is strictly dependent on the covalent, peptide-mediated targeting of ^{177}Lu to HSPB1-expressing tumors. Immunohistochemistry analysis of HSPB1 expression in both PDX and orthotopic rectal tumor models revealed strong HSPB1 staining in subcutaneous and PDX tumor tissues (Fig. S15 in the ESM), corroborating radiotracer uptake patterns observed in SPECT/CT imaging. To evaluate therapeutic efficacy, we conducted a systematic treatment study using BALB/c mice bearing subcutaneous CT26-HSPB1 tumors. Mice were randomly assigned to five groups: G1: PBS, G2: 20 nM DPTP, G3: 14.8 MBq free ^{177}Lu, G4: 7.4 MBq ^{177}Lu-DPTP, G5: 14.8 MBq ^{177}Lu-DPTP. Tumor volumes were measured every two days post-injection. Compared with free ^{177}Lu and DPTP alone, ^{177}Lu-DPTP significantly suppressed tumor growth and prolonged survival in a dose-dependent manner (Figs. 6(d) and 6(e)). To evaluate treatment safety, mouse body weight was monitored throughout the study, and no significant changes were observed (Fig. 6(f)). Histopathological examination of tumors from different groups revealed extensive cellular damage and apoptosis in tumors treated with 14.8 MBq ^{177}Lu-DPTP, indicating a robust anti-tumor effect (Fig. 6(g)). To further assess safety, heart, liver, spleen, lung, kidney, and blood samples were collected 30 days post-treatment from the 14.8 MBq ^{177}Lu-DPTP group for biochemical and hematological analysis. No significant differences were observed compared to control groups, and no signs of radiation induced toxicity were detected (Figs. S16(a) and S16(b) in the ESM). Together, these findings demonstrate that ^{177}Lu-DPTP not only exhibits potent anti-tumor activity in both PDX and low rectal tumor models but also possesses excellent biocompatibility and safety, supporting its potential for clinical translation in early diagnosis and targeted radionuclide therapy of colorectal cancer.

3 Discussion

CRC is one of the most prevalent malignancies worldwide. Despite continuous advancements in screening strategies, early diagnosis and precision therapy remain major clinical challenges. Current understanding of CRC pathogenesis emphasizes the adenoma-carcinoma sequence as the principal pathway of tumorigenesis. However, the key molecular mechanisms driving this transition are still not fully elucidated. In this study, through retrospective clinical analysis and proteomic profiling, we characterized the malignant transformation potential of distinct adenoma subtypes, and for the first time, systematically revealed the pivotal role of the small heat shock protein HSPB1 in the adenoma-to-carcinoma transition. Recent studies have shown that members of the heat shock protein (HSP) family play critical roles in tumor progression. HSPB1, as a prominent member of this family, has been reported to correlate with poor prognosis and therapeutic resistance across various malignancies. Furthermore, accumulating evidence indicates that HSPB1 regulates cell proliferation, migration, invasion, and reshaping of the tumor microenvironment [26, 27, 35, 36]. Consistent with these findings, our results demonstrate that HSPB1 is significantly upregulated during the malignant transformation of adenomas and in CRC tissues, supporting its potential role as a key oncogenic driver and providing a strong theoretical basis for its use as an early diagnostic biomarker.

Currently, the detection of high-risk adenomas and early-stage CRC predominantly depends on traditional colonoscopy and imaging. Nevertheless, these methods face limitations, including invasiveness, suboptimal patient compliance, and inadequate sensitivity for early lesions [37, 38]. In contrast, molecular imaging using targeted probes has emerged as a promising tool for non-invasive cancer detection due to its high sensitivity and specificity [39, 40]. Among them, theranostic radiopharmaceuticals labeled with ^{177}Lu have shown significant success in solid tumors such as prostate and neuroendocrine cancers [41, 42]. Therefore, developing a radiolabeled peptide probe targeting HSPB1 could offer a novel breakthrough in the early diagnosis and treatment of CRC. In this study, we rationally designed three ^{177}Lu-labeled peptide probes (DTP, DITP, and DPTP) based on a high-affinity HSPB1-binding peptide. Through structural modifications including PEGylation and 4-(p-iodophenyl) butyric acid conjugation, we significantly improved the pharmacokinetic profiles and targeting performance of these probes. Among them, ^{177}Lu-DPTP exhibited exceptional tumor selectivity and imaging contrast in both CRC-PDX and orthotopic low rectal cancer models. Importantly, it also demonstrated potent dose-dependent anti-tumor effects without eliciting systemic toxicity. These results validate the clinical feasibility and translational potential of an HSPB1-targeted theranostic strategy.

Nevertheless, this study has several limitations. This study has certain limitations. First, the diagnostic performance of HSPB1 requires validation in larger clinical cohorts. Second, despite promising preclinical results, translational challenges such as potential immunogenicity and interspecies metabolic differences need to be addressed. Furthermore, integrating emerging PET imaging radionuclides such as ^{68}Ga and ^{89}Zr may help further enhance imaging resolution and clinical applicability [43, 44]. In summary, this study is the first to establish the critical regulatory role of HSPB1 in the malignant transformation of colorectal adenomas and to develop an effective HSPB1-targeted radiolabeled theranostic probe, ^{177}Lu-DPTP. This innovative approach provides not only a new molecular target and platform for early diagnosis and precision therapy of CRC but also a research paradigm for screening and treating other solid tumors.

4 Conclusions

Through long term clinical cohort analysis combined with proteomics, we identified HSPB1 as a key driver in the progression from colorectal adenoma to carcinoma. HSPB1 was found to be significantly upregulated in high risk adenoma subtypes and early stage CRC tissues, with its expression closely associated with enhanced cell proliferation, migration, and invasion. Leveraging the functional relevance of HSPB1, we designed a series of radiolabeled peptide probes. Through iterative structural optimization, we ultimately developed ^{177}Lu-DPTP, which exhibits high affinity for HSPB1 and favorable pharmacokinetic properties. *In vivo* experiments demonstrated that ^{177}Lu-DPTP selectively accumulated in HSPB1-overexpressing tumors, enabled high-contrast SPECT/CT imaging, and effectively inhibited tumor growth in both PDX and orthotopic low rectal cancer models. Importantly, ^{177}Lu-DPTP achieved significant therapeutic efficacy without inducing systemic toxicity, indicating good biocompatibility and safety.

Overall, we present a novel HSPB1-targeted theranostic strategy that not only offers a reliable tool for early precision imaging of CRC but also establishes a new molecular target and technical platform for radiotherapeutic intervention, with promising clinical translation potential.

Electronic Supplementary Material: Supplementary material (peptide synthesis, radiolabeling procedures, cell culture, establishment of stable cell lines, and all experimental assays, and tables of clinical cohort analysis, adenoma transformation statistics, and differentially expressed proteins) is available in the online version of this article at https://doi.org/10.26599/NR.2026.94908439.

Data availability

All data needed to support the conclusions in the paper are presented in the manuscript and/or the Electronic Supplementary Material. Additional data related to this paper may be requested from the corresponding author upon request.

Acknowledgements

This work was partially supported by the National Natural Science Foundation of China (No. 32371461), Key Laboratory of Radiation Damage and Treatment of Jiangsu Provincial Universities and Colleges, Suzhou Fundamental Research Project (No. SJC2023001), and the Project Funded by the Priority Academic Program Development of Jiangsu Higher Education Institutions (PAPD).

Declaration of competing interest

All the contributing authors report no conflict of interests in this work.

Author contribution statement

S. L., Y. H. W., and M. M. X are contributed equally to this work. S. L. and Y. H. W. designed the experiments. S. L., C. H. Z., X. L. Y., H. Y., and F. P. performed the experiments. M. M. X. conducted the bioinformatics analysis. W. F. L. performed the molecular docking. J. D. L. and T. L. performed the manuscript proofreading. K. Y. and L. H. conceptualized the study, supervised the research, acquired funding, and provided project administration, served as the corresponding author.

Informed consent

The requirement for written informed consent was waived by the Institutional Ethics Committee of the First Affiliated Hospital of Soochow University (authorisation number ECSU-2019000212), due to the retrospective nature of the study and the use of anonymized data.

Ethics statement

The animals were used according to the protocol approved by the Laboratory Animal Center of Soochow University (Ethics Number: 202410A0403). The use of human tissue was approval from the Institutional Ethics Committee of the First Affiliated Hospital of Soochow University (authorisation number ECSU-2019000212).

Use of AI statement

None.

References

[1] Bray, F.; Laversanne, M.; Sung, H.; Ferlay, J.; Siegel, R. L.; Soerjomataram, I.; Jemal, A. Global cancer statistics 2022: GLOBOCAN estimates of incidence and mortality worldwide for 36 cancers in 185 countries. *CA Cancer J. Clin.* **2024**, *74*, 229–263.

[2] Akimoto, N.; Ugai, T.; Zhong, R.; Hamada, T.; Fujiyoshi, K.; Giannakis, M.; Wu, K. N.; Cao, Y.; Ng, K.; Ogino, S. Rising incidence of early-onset colorectal cancer-a call to action. *Nat. Rev. Clin. Oncol.* **2021**, *18*, 230–243.

[3] Mizutani, T.; Boretto, M.; Clevers, H. Modeling adenoma-carcinoma progression from a single *MLH1*-knockout cell via colon organoids. *Nat. Cancer* **2024**, *5*, 1798–1799.

[4] Cui, G. L.; Li, Z. F.; Florholmen, J.; Goll, R. Dynamic stromal cellular reaction throughout human colorectal adenoma-carcinoma sequence: A role of TH17/IL-17A. *Biomed. Pharmacother.* **2021**, *140*, 111761.

[5] Shen, J. H.; Hu, L.; Yang, L.; Zhang, M. S.; Sun, W. H.; Lu, X. M.; Lin, G. F.; Huang, C.; Zhang, X. R.; Chin, Y. E. Reversible acetylation modulates dishevelled-2 puncta formation in canonical Wnt signaling activation. *Signal Transduct. Target. Ther.* **2020**, *5*, 115.

[6] Shaukat, A.; Levin, T. R. Current and future colorectal cancer screening strategies. *Nat. Rev. Gastroenterol. Hepatol.* **2022**, *19*, 521–531.

[7] Lee, M. W.; Pourmorady, J. S.; Laine, L. Use of fecal occult blood testing as a diagnostic tool for clinical indications: A systematic review and meta-analysis. *Am. J. Gastroenterol.* **2020**, *115*, 662–670.

[8] Pickhardt, P. J.; Hassan, C.; Halligan, S.; Marmo, R. Colorectal cancer: CT colonography and colonoscopy for detection-systematic review and meta-analysis. *Radiology* **2011**, *259*, 393–405.

[9] Chen, S. R.; Shi, X. M.; Liu, S.; Pei, P.; Yang, K.; Hu, L. Advancements in colorectal cancer detection: The role of immuno-positron emission tomography, immuno-single-photon emission computed tomography, and machine learning applications. *J. Intell. Med.* **2024**, *1*, 63–90.

[10] Nakamura, K.; Hernández, G.; Sharma, G. G.; Wada, Y.; Banwait, J. K.; González, N.; Perea, J.; Balaguer, F.; Takamaru, H.; Saito, Y. et al. A liquid biopsy signature for the detection of patients with early-onset colorectal cancer. *Gastroenterology* **2022**, *163*, 1242–1251.E2.

[11] Zhou, H.; Zhu, L. Y.; Song, J.; Wang, G. H.; Li, P. Z.; Li, W. Z.; Luo, P.; Sun, X. L.; Wu, J.; Liu, Y. Z. et al. Liquid biopsy at the frontier of detection, prognosis and progression monitoring in colorectal cancer. *Mol. Cancer* **2022**, *21*, 86.

[12] Chang, W. Y.; Liao, W. C.; Chang, L. C.; Lin, H. H.; Wei, P. Y.; Wu, H. C.; Chiu, H. M.; Wu, M. S. Comparison of adenoma detection rate between three-dimensional and standard colonoscopy: A multicenter randomized controlled trial. *Endoscopy* **2025**, *57*, 1085–1094.

[13] Tursi, A. The role of colonoscopy in managing diverticular disease of the colon. *J. Gastrointestin. Liver Dis.* **2015**, *24*, 85–93.

[14] Shi, X. M.; Liu, T.; Pei, P.; Shen, W. H.; Hu, L.; Zhu, R.; Wang, F.; Chen, C. Y.; Yang, K. Radionuclide-labeled antisilencing function 1a inhibitory peptides for tumor identification and individualized therapy. *ACS Nano* **2024**, *18*, 9114–9127.

[15] Wei, W. J.; Rosenkrans, Z. T.; Liu, J. J.; Huang, G.; Luo, Q. Y.; Cai, W. B. ImmunoPET: Concept, design, and applications. *Chem. Rev.* **2020**, *120*, 3787–3851.

[16] Chen, Y. M.; Liu, X. W.; Sun, Y.; Liu, K. Y.; Ding, D.; Song, S. L.; Tan, W. H. Noninvasive molecular imaging using anti-Trop-2 aptamer for targeted therapy of small cell lung cancer. *J. Nanobiotechnol.* **2025**, *23*, 182.

[17] Han, T. T.; Quan, Z. Y.; Wei, H. L.; Zhang, M. R.; Ye, J. J.; Li, G. Y.; Wang, J. L.; Ma, T. Q.; Wang, J.; Kang, F. Diagnostic value of [^{18}F]-FDG and [^{68}Ga]-FAPI-04 PET/MRI for lymph node metastasis in papillary thyroid cancer. *Mol. Imaging Biol.* **2025**, *27*, 540–549.

[18] Lwin, T. M.; Minnix, M.; Li, L.; Sherman, A.; Hong, T.; Wong, J. Y. C.; Olafsen, T.; Poku, E.; Bouvet, M.; Fong, Y. et al. Multimodality PET and near-infrared fluorescence intraoperative imaging of CEA-positive colorectal cancer. *Mol. Imaging Biol.* **2023**, *25*, 727–734.
[19] Maleki, F.; Masteri Farahani, A.; Sadeghzadeh, N.; Mardanshahi, A.; Abediankenari, S. Preparation and evaluation of ^{99m}Tc-HYNIC-$_D$(TPPE) as a new targeted imaging probe for detection of colon cancer: Preclinical comparison with ^{99m}Tc-HYNIC-EPPT. *Chem. Biol. Drug Des.* **2020**, *96*, 1223–1231.
[20] Liu, Y.; Yao, X. B.; Wang, C. X.; Wang, M. R.; Wang, Y.; Ye, M. S.; Liu, Y. Peptide-based ^{68}Ga-PET radiotracer for imaging CD133 expression in colorectal cancer. *Nucl. Med. Commun.* **2021**, *42*, 1144–1150.
[21] Gollub, M. J.; Grewal, R. K.; Panu, N.; Thipphavong, S.; Sohn, M.; Zheng, J.; Moskowitz, C. S. Diagnostic accuracy of ^{18}F-FDG PET/CT for detection of advanced colorectal adenoma. *Clin. Radiol.* **2014**, *69*, 611–618.
[22] Xu, W. M.; Li, H. S.; Guo, Z. Q.; Zhang, L. Q.; Zhang, R. S.; Zhang, L. Combined SUVmax and localized colonic wall thickening parameters to identify high-risk lesions from incidental focal colorectal ^{18}F-FDG uptake foci. *Front. Oncol.* **2022**, *12*, 972096.
[23] Yang, W. H.; Gao, K. P.; Qian, Y. H.; Huang, Y. Y.; Xiang, Q.; Chen, C.; Chen, Q. Q.; Wang, Y. L.; Fang, F. Y.; He, Q. H. et al. A novel tRNA-derived fragment AS-tDR-007333 promotes the malignancy of NSCLC via the HSPB1/MED29 and ELK4/MED29 axes. *J. Hematol. Oncol.* **2022**, *15*, 53.
[24] Peng, S. F.; Yin, Y. H.; Zhang, Y. Z.; Zhu, F.; Yang, G.; Fu, Y. FYN/TOPK/HSPB1 axis facilitates the proliferation and metastasis of gastric cancer. *J. Exp. Clin. Cancer Res.* **2023**, *42*, 80.
[25] Liang, Y. R.; Wang, Y. J.; Zhang, Y.; Ye, F. Z.; Luo, D.; Li, Y. M.; Jin, Y. H.; Han, D. W.; Wang, Z. K.; Chen, B. et al. HSPB1 facilitates chemoresistance through inhibiting ferroptotic cancer cell death and regulating NF-κB signaling pathway in breast cancer. *Cell Death Dis.* **2023**, *14*, 434
[26] Henriques, A.; Koliaraki, V.; Kollias, G. Mesenchymal MAPKAPK2/HSP27 drives intestinal carcinogenesis. *Proc. Natl. Acad. Sci. USA* **2018**, *115*, E5546–E5555.
[27] Yang, Y.; Bao, Y.; Yang, G. K.; Wan, J.; Du, L. J.; Ma, Z. H. MiR-214 sensitizes human colon cancer cells to 5-FU by targeting Hsp27. *Cell. Mol. Biol. Lett.* **2019**, *24*, 22.
[28] Wang, W. Z.; Hu, Z. Y. Targeting peptide-based probes for molecular imaging and diagnosis. *Adv. Mater.* **2019**, *31*, 1804827.
[29] Gibert, B.; Hadchity, E.; Czekalla, A.; Aloy, M. T.; Colas, P.; Rodriguez-Lafrasse, C.; Arrigo, A. P.; Diaz-Latoud, C. Inhibition of heat shock protein 27 (HspB1) tumorigenic functions by peptide aptamers. *Oncogene* **2011**, *30*, 3672–3681.
[30] Müller, C.; Struthers, H.; Winiger, C.; Zhernosekov, K.; Schibli, R. DOTA conjugate with an albumin-binding entity enables the first folic acid-targeted ^{177}Lu-radionuclide tumor therapy in mice. *J. Nucl. Med.* **2013**, *54*, 124–131.
[31] Greschner, A. A.; Brahiti, N.; Auger, M.; Hu, L.; Soleymani Abyaneh, H.; Barbeau, X.; Parent, V.; Gaillet, B.; Guay, D.; Soultan, A. H. et al. PEGylation of a peptide-based amphiphilic delivery agent and influence on protein delivery to cells. *Biomacromolecules* **2023**, *24*, 4890–4900.
[32] Li, Z.; Zhu, Y. B.; Zeng, H. W.; Wang, C.; Xu, C.; Wang, Q.; Wang, H. M.; Li, S. Y.; Chen, J. T.; Xiao, C. et al. Mechano-boosting nanomedicine antitumour efficacy by blocking the reticuloendothelial system with stiff nanogels. *Nat. Commun.* **2023**, *14*, 1437.
[33] Wang, Y. F.; Dong, A. Q.; Man, J. P.; Chen, H.; Shen, W. H.; Wang, L.; Yang, H. L.; Hu, L.; Yang, K. TREM2 scFv-engineering *Escherichia coli* displaying modulation of macrophages to boost cancer radio-immunotherapy. *Adv. Mater.* **2025**, *37*, 2417920
[34] Blanchard, Z.; Brown, E. A.; Ghazaryan, A.; Welm, A. L. PDX models for functional precision oncology and discovery science. *Nat. Rev. Cancer* **2025**, *25*, 153–166.
[35] Tweedle, E. M.; Khattak, I.; Ang, C. W.; Nedjadi, T.; Jenkins, R.; Park, B. K.; Kalirai, H.; Dodson, A.; Azadeh, B.; Terlizzo, M. et al. Low molecular weight heat shock protein HSP27 is a prognostic indicator in rectal cancer but not colon cancer. *Gut* **2010**, *59*, 1501–1510.
[36] Wang, Y.; Lu, Z.; Wang, N. N.; Feng, J. Z.; Zhang, J. J.; Luan, L.; Zhao, W.; Zeng, X. D. Long noncoding RNA DANCR promotes colorectal cancer proliferation and metastasis via miR-577 sponging. *Exp. Mol. Med.* **2018**, *50*, 1–17.
[37] Hoffmeister, M.; Holleczek, B.; Stock, C.; Zwink, N.; Stolz, T.; Stegmaier, C.; Brenner, H. Utilization and determinants of follow-up colonoscopies within 6 years after screening colonoscopy: Prospective cohort study. *Int. J. Cancer* **2019**, *144*, 402–410.
[38] Knudsen, M. D.; Wang, K.; Wang, L.; Polychronidis, G.; Berstad, P.; Hjartåker, A.; Fang, Z.; Ogino, S.; Chan, A. T.; Song, M. Y. Colorectal cancer incidence and mortality after negative colonoscopy screening results. *JAMA Oncol.* **2025**, *11*, 46–54.
[39] Monteil, J.; Le Brun-Ly, V.; Cachin, F.; Zasadny, X.; Seitz, J. F.; Mundler, O.; Selvy, M.; Smith, D.; Rullier, E.; Lavau-Denes, S. et al. Comparison of ^{18}FDG-PET/CT and conventional follow-up methods in colorectal cancer: A randomised prospective study. *Dig. Liver Dis.* **2021**, *53*, 231–237.
[40] Zhao, L. S.; Ge, J. X.; Zhang, R. R.; Wang, H.; Liu, X. Y.; Xu, K. D.; Liu, Y. J.; Zhao, W. C.; Zhang, W. G.; Ye, L. et al. Noninvasive immunotyping and immunotherapy monitoring of lung cancers via nuclear imaging of LAG-3 and PD-L1. *Adv. Sci.* **2025**, *12*, 2404231.
[41] Parghane, R. V.; Talole, S.; Prabhash, K.; Basu, S. Clinical response profile of metastatic/advanced pulmonary neuroendocrine tumors to peptide receptor radionuclide therapy with ^{177}Lu-DOTATATE. *Clin. Nucl. Med.* **2017**, *42*, 428–435.
[42] Usmani, S.; Rasheed, R.; Ahmed, N.; Omar, Y.; Numani, S. P. Targeted peptide receptor radionuclide therapy with ^{177}Lu-DOTATATE alters joints inflammation. *Clin. Nucl. Med.* **2025**, *50*, e102–e104.
[43] Bauman, A.; Valverde, I. E.; Fischer, C. A.; Vomstein, S.; Mindt, T. L. Development of ^{68}Ga- and ^{89}Zr-labeled exendin-4 as potential radiotracers for the imaging of insulinomas by PET. *J. Nucl. Med.* **2015**, *56*, 1569–1574.
[44] Soydal, C.; Demir, B.; Akkus Gunduz, P.; Baltacioglu, M. H.; Araz, M.; Kuru Oz, D.; Kucuk, N. O. ^{68}Ga DOTATATE PET/MR imaging of well-differentiated primary and metastatic liver neuroendocrine tumors: Unified evaluation and correlations of PET, DCE, DWI, and T2-weighted images. *Clin. Nucl. Med.* **2025**, *50*, e531–e542.